Calibration methodology of static, dynamic and ageing parameters of an electrochemical model for a Li-ion cell based on an experimental approach

Renewable Energy 246 (2025) 122793

Contents lists available at ScienceDirect

Renewable Energy

journal homepage: www.elsevier.com/locate/renene

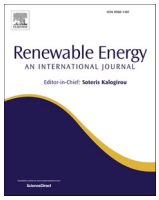

Calibration methodology of static, dynamic and ageing parameters of an electrochemical model for a Li-ion cell based on an experimental approach

Francesco Mazzeo [a,*], Eduardo Graziano [b], Silvia Bodoardo [c], Davide Papurello [d]

[a] DIMEAS, Department of Mechanical and Aerospace Engineering, Politecnico di Torino, Corso Duca degli Abruzzi, 24, 10129, Turin, Italy
[b] Powertech Engineering Srl, Italy
[c] Department of Applied Science and Technology (DISAT), Politecnico di Torino, Corso Duca degli Abruzzi, 24, 10100, Turin, Italy
[d] Energy Center, Politecnico di Torino, Via Paolo Borsellino 38/16, 10138, Turin, Italy

A B S T R A C T

This study presents a novel methodology for developing a digital twin of a lithium-ion coin cell battery (Graphite-NMC622), accurately replicating the average discharge behaviour of various laboratory-tested batteries and characterizing degradation phenomena through cyclic ageing experiments. Given the anticipated rise in electric vehicle adoption, this work is particularly relevant for addressing the growing demand for lithium-ion batteries. The experimental characterization identified the minimum requirements for battery modelling, with tests conducted up to a C/5 current. Degradation behaviours were analysed through cycle ageing tests at two State-Of-Charge (SOC) ranges (100 %–0 % and 90 %–10 %), establishing a robust foundation for modelling degradation trends. While further calendar ageing tests could enhance the degradation modelling, they would require extensive data and time. Despite these constraints, the virtual coin cell model developed using GT-AutoLion, an industry-standard CAE software, demonstrated excellent accuracy, achieving an RRMSE of less than 2.0 % and R^2 greater than 0.95. This work is significant as it provides a reliable framework for battery modelling that can assist companies in optimizing battery design and performance.

1. Introduction

The automotive industry has faced a paradigm shift towards sustainable mobility to reduce pollutant emissions and dependence on fossil fuels [1,2]. Emissions from the transport sector have grown at an average annual rate of 1.7 per cent since 1990. This growth is the highest of any sector [3]. An increase in the total final consumption of oil implies, despite the production of increasingly efficient transportation systems, a growth in the production of CO_2, for which the transport system is responsible for 24 % of direct emissions from fuel combustion. The IEA has created a sustainable scenario that runs through 2030 that can perfectly comply with the Paris Agreement by keeping the global average temperature rise below 2 °C. This scenario also includes a reduction in emissions from the transportation sector, among which the largest contribution comes from road passenger vehicles. To achieve a reduction in emissions, it is necessary to increase the number of vehicles powered by alternative fuels such as hydrogen or bioethanol and, of course, batteries [2,4–6]. In the last decade, there has been a significant surge in the adoption of electric vehicles, with approximately 10 million of them being driven worldwide by the end of 2020. These numbers are set to increase and, according to the IEA's EV outlook, will exceed 24 % of the market shar for light duty vehicles in 2030 [7]. The main criticisms that can be observed for LIBs used in electric vehicles refer to the Thermal Runaway (TR) phenomenon as reported in the literature [8–11]. A significant amount of effort has been dedicated to mitigating and preventing this phenomenon. Feng et al. [9] proposed a time-sequence map to clarify the thermal runaway mechanism, offering insights into the state transitions that drive failure during tests. Yang et al. [10], highlighted challenges in battery safety, including limited progress in safer battery development, difficulty in identifying and predicting coupled faults, and inefficiencies in fault warning algorithms for practical applications. They emphasized the need for advanced warning systems, improved battery designs, and specialized fire extinguishing agents to address EV fire risks effectively. The TR phenomenon can be triggered mainly by three causes: electrical, mechanical, and thermal [9,12]. Rojas et al. [12], studied three typical TR trigger modes (heating the LIB module, penetrating the module with a nail and overcharging the module). They found that the trigger time is minimal as far as penetration with the needle system is concerned, while it turns out to be a function of current electrical overload. It has been identified how the percentage of thermal energy released by the TR could be controlled by co-injecting it appropriately through the structure of the battery pack [12]. Research also focuses, with different methods, mostly on the control of thermal energy generated during the operation of the battery pack. Kumar et al. [13], highlighted that the Battery Thermal Management System based on phase change materials and heat pipes were found to be more effective than air and water cooling. Thermal control

* Corresponding author.
E-mail addresses: francesco.mazzeo@polito.it (F. Mazzeo), davide.papurello@polito.it (D. Papurello).

https://doi.org/10.1016/j.renene.2025.122793
Received 9 November 2024; Received in revised form 9 January 2025; Accepted 1 March 2025
Available online 13 March 2025

Nomenclature

A (cm^2) Electrode surface area
AMI Active Material Isolation
BMS Battery Management System
CAE Computer-Aided Engineering
CEI Cathode Electrolyte Interface
DOD Depth Of Discharge
D_s (m^2/s) Lithium-ion diffusion coefficient in the solid phase
D_e (m^2/s) Lithium-ion diffusion coefficient in the liquid phase
D_{an} (m^2/s) Lithium-ion diffusion coefficient in the anode electrode
D_{cat} (m^2/s) Lithium-ion diffusion coefficient in the cathode electrode
EDL: Electrical Double Layer
E_{SEI} (J/mol) SEI layer growth activation energy
E_{CEI} (J/mol) CEI layer growth activation energy
$E_{EC,An}$ (J/mol) Anode EC diffusivity degradation activation energy
$E_{EC,Cat}$ (J/mol) Cathode EC diffusivity degradation activation energy
$E_{AMI,An}$ (J/mol) Anode active material isolation activation energy
$E_{AMI,Cat}$ (J/mol) Cathode active material isolation activation energy
FCC^{Ca} (mAh/g) Cathode first charge capacity
FCC^{An} (mAh/g) Anode first charge capacity
FDC^{Ca} (mAh/g) Cathode first discharge capacity
FDC^{An} (mAh/g) Anode first discharge capacity
I (A) Current
i_0 (A/m^2) Exchange current density
LIB Lithium-Ion Battery
$Loading^{Ca}$ (mAh/cm^2) Cathode capacity loading
NMC Nickel, manganese and cobalt
N/P (−) Ratio between anode and cathode capacity loading
p_{i0} (−) multiplicative coefficient of cathode exchange current density
p_{Dan} (−) multiplicative coefficient of the lithium-ion diffusion coefficient in the anode electrode
p_{DCat} (−) multiplicative coefficient of the lithium-ion diffusion coefficient in the cathode electrode
R_c ($m\Omega\ cm^2$) Contact resistance
RMS Root Mean Square
RRMSE Relative Root Mean Square Error
SOC (−) State of Charge
SOH (−) State of Health
SEI Solid Electrolyte Interface
TFC Total Final Consumption
TR Thermal Runaway
U^{Ca}_{max} (V) Maximum cathode open circuit potential
$V_{\exp}$ (V) Experimental voltage
V_{sim} (V) Simulation voltage
V_{act} (V) Activation overvoltage
V_{ohm} (V) Ohmic overvoltage
V_{conc} (V) Concentration overvoltage
ϕ_s (V) surface voltage
ψ_{SEI} (−) SEI layer growth reference value
ψ_{CEI} (−) CEI layer growth reference value
$\psi_{EC,An}$ (−) Anode electrolyte diffusivity degradation reference value
$\psi_{EC,Cat}$ (−) Cathode electrolyte diffusivity degradation reference value
$\psi_{AMI,An}$ (−) Anode active material isolation reference value
$\psi_{AMI,Cat}$(−) Cathode active material isolation reference value

by heat pipes is found to be preferable because it is lighter. Liang et al. [14], demonstrated that the maximum temperature and temperature difference of a battery can be effectively controlled within the desired range using intermittent cooling. Notably, the battery's thermal response under intermittent cooling is comparable to that of constant cooling. This finding highlights the potential of intermittent cooling to reduce the power consumption of Battery Thermal Management Systems (BTMS) by minimizing their operating time. The complexity of thermal management is only one aspect of LIBs, which is onerous in terms of experimental costs for validating CFD models. Other characteristic aspects of LIBs must be addressed to ensure safe and continuous operation over time, especially considering the TR. For these reasons, an innovative approach that can implement a digital twin of a LIB system could confer interesting answers to better address LIB management issues, make them integrable into battery packs, and enable effective simulation with low computational costs. The calibration and optimization of the model are based on a data-driven technique and electrochemical models implemented on the software GT-AutoLion. Among the various electrochemical models, the one exploited by the GT-AutoLion software is the "Pseudo 2D" (P2D) electrochemical model for Lithium-ion (Li-ion) batteries, the basis of most electrochemical models for many years [15]. Recently, many researchers have been relying on this software for their work and studies, proving to be a very reliable and concrete alternative for modelling lithium-ion batteries [16–19], this is because it offers high flexibility and ease in modifying the model parameters thanks to an intuitive interface. The software significantly saves time in conducting studies compared to other open-source software [20]. However, the drawback is that it is a paid tool. Natarajan et al. [17] developed an electrochemistry-based cell model using GT-AutoLion to simulate and validate the performance of two commercially available Lithium Iron Phosphate (LiFePO4) and Nickel Cobalt Aluminum (NCA) cells. While, Chopra et al. [19], explored the implementation of a detailed electro-thermal P2D battery model, developed in GT-AutoLion, in combination with a 1D vehicle model to predict the performance and aging of an electric vehicle (EV) system over 40 weeks of operation. Physics-based models (such as the P2D) are increasingly used in the development of next-generation BMSs thanks to the application of model order reduction techniques to reduce computational costs, as highlighted by Li et al. [21] in their work. The P2D model discretizes the Lithium-ion cell's governing equations using the finite control volume approach: the Cathode, Separator, and Anode are discretized in the "thickness" direction. In each finite control volume of the Cathode and Separator, there is a spherical representation of the active material, each of which is discretized into constant volumes in the radial direction. This model is composed of a set of parameters including cell design specifications and material properties, the most influential parameter identification and calibration play a fundamental role in the model's predictability and accuracy. The optimization process is based on heuristic techniques such as genetic algorithms [22], a particular objective function is defined, in this case, the root means square error between the experimental data and the model output, which will be minimized using the chosen algorithm acting on the pre-mentioned calibration parameters. Often the electrochemical model is coupled with a thermal model to investigate heat generation and dissipation rates and predict the temperature change of the cell [23] which has an influence on his performance [24], but in this case, dealing with small coin cells with metal cases and being that the maximum current used for the digital-twin calibration is C/5, it has been verified that the temperature increase is negligible during tests at ambient temperature while in the other cases, the temperature was controlled in a climatic chamber. This work presents a novel approach to creating a "digital twin" of a lithium-ion coin cell battery. The main innovation lies in two contributions: first, the definition of a minimum set of experimental tests required to construct a sufficiently accurate digital twin; and second, the development of a precise calibration procedure for the electrochemical model in GT-AutoLion. This calibration is based on discharge curves to model

performance and cycle aging tests to capture degradation, utilizing GT-AutoLion, a software widely adopted in the industry, thereby enhancing the practical applicability of this approach.

By refining the calibration of both performance and degradation within this framework, this study establishes a highly reliable digital twin. The validated model not only enables the safe testing of lithium-ion batteries under critical conditions but also provides a valuable tool for optimizing battery design and testing protocols in the industry.

2. Materials and methods

2.1. Battery creation

The batteries used are coin cells assembled manually in the laboratory and composed of NMC622 as cathode, graphite as anode, a polymeric membrane (Celgard 2325) as the separator, $LiPF_6$ as the electrolyte in liquid form and aluminium and copper as the current collector for cathode and anode respectively, with a maximum voltage of 4.20 V (OCV), see Table 1 and Fig. 1. Sample materials were bought from (Xiamen AOT Electronics technology co., ltd., China). In the process of creation, particular attention must be paid to aligning all the elements that make up the geometry of the cell to obtain maximum performance. To have a larger statistical sample, various coin cells were created and tested, and the average discharge curve was used as experimental input on the GT-AutoLion model for the characterization of the digital twin. The assembly takes place inside the "glovebox", a sealed container, specially designed and built to handle instruments and substances in a confined environment separate from that in which the operator is located (Iteco Engineering, Ra, Italy). The glovebox is necessary to avoid the interaction of electrolytes that contain lithium with oxygen and nitrogen present in the atmosphere, giving rise to reactions that can cause deterioration of performance or more dangerous ones such as fires [25]. Once the battery is created, the container is placed in an automatic press where it is sealed at a pressure of 5.5 bar (Sovema, Vr, Italy). Various assemblies have been tested to identify the best-performing one that would achieve a higher C-RATE during discharge, focusing on determining the proper electrode dimensions to prevent short circuits and ensure optimal performance, as well as the number of springs or spacers required to maintain reliable contact among the various layers. The best one is shown in Fig. 1, while the geometric dimensions of the various layers are shown in Table 1. Once assembled, the coin cells are inserted into an ultra-high precision charge/discharge cycler (Models: BT-G-25 and IBT21084LC, Arbin Instruments, USA), which can provide a constant charge and discharge current corresponding to the desired C-rates. Each coin cell then undergoes a startup procedure consisting of three formation cycles (charge/discharge) at a low current of C/20. Since the capacity of the battery is not known before testing it, to calculate the currents corresponding to the desired C-RATEs, it was decided to use the electrode with the lowest ideal specific capacity, i.e., NMC622 (see Table 1). During the creation of the coin-cell, the NMC622 disk was weighted, and the battery capacity was calculated; from the latter, the currents expressed in C-RATE, used in the cycler, were derived. At the end of the formation cycles, the effective capacity of the coin cell can be calculated, and the current can be adjusted. Coin cells with significantly different capacity values are discarded. To obtain the necessary data to create a digital twin, the experimental campaign was divided into two parts. The first can be called characterisation tests whose aim is to obtain discharge voltage curves at different currents and temperatures, while the second part is cyclic ageing to obtain SOH curves to calibrate degradation phenomena.

Table 1
Battery materials and geometric dimensions (Xiamen AOT Electronics technology co., ltd., China).

Components	Materials	Capacity [mAh/g]	Diameter [mm]	Thickness [μm]
Spacers	Stainless steel	–	15.5	500
Neg. electrode	Copper and graphite	350	18	87
Separator	Celgard 2325	–	20	20
Electrolyte	$LiPF_6$	–	–	–
Pos. electrode	Aluminum and NMC622	175	15	77

2.2. Characterization tests

The coin cells are inserted into the Arbin cycler, where a constant charge and discharge current corresponding to the desired C-rates of C/20, C/10, and C/5 is applied between two predefined states of charge: SOC = 0 % and SOC = 100 %. It was decided not to exceed C/5 due to the limited performance of the coin cells. For each C-rate, multiple charge and discharge cycles were conducted on different coin cells. Cells showing similar discharge trends (voltage-capacitance curves) were selected to calculate the average curves, which are presented in Fig. 1 for two specific temperature conditions: room temperature and 45 °C. The room temperature condition was 26 °C, with the temperature monitored by a thermocouple placed on the upper casing of the cell to ensure consistency throughout the tests. The measured temperature fluctuations were negligible (on the order of 1 °C) and thus had no significant impact on performance, allowing us to consider the temperature effectively constant. For the 45 °C condition, the experiments were performed in a climate chamber (Binder KBF-S 115, Binder GmbH, Germany) to maintain precise temperature control. Eight different coin cells were tested: at 26 °C and 45 °C. Fig. 2 illustrates that as the C-rate increases, there is a corresponding reduction in discharge capacity as higher current rates limit the effective utilization of active materials and increase internal resistance within the cell, reducing the overall accessible capacity. Additionally, improved performance is observed at 45 °C for the same C-rate. This enhancement is attributed to the favourable effects of higher temperatures on electrode kinetics, ionic conductivity, and diffusive phenomena [26].

2.3. Cycle ageing tests

During its use, the battery is subject to degradation phenomena that can be either mechanical or chemical, leading to a reduction in useful capacity [27]. One of the main effects of battery ageing is the degradation of the electrode, which can then lose active material that dissolves into the electrolyte, such as manganese [28]. In any case, the degradation mechanisms are multiple and different between positive and negative electrodes and are strongly favoured by high temperatures and charge states (SOC>80 %) [29,30]. To estimate the effect of these phenomena, it was decided to use the cyclic ageing test at an ambient temperature of 26 °C. The methodology is a readaptation of the procedure developed by ENEA (National Agency for New Technologies, Energy and Sustainable Economic Development) [31], as non-commercial batteries, and consists of constant current (CC) charge and discharge cycles carried out at C-RATE of C/10 and C/5, respectively, and can be summarized as follows. Three formation cycles (full charge and discharge) at C/20 from which the initial specific capacity (mAh/g) is calculated.

1. From the last discharge cycle, the voltage corresponding to the desired minimum SOC is calculated.
2. From the last charge cycle, the voltage corresponding to the desired maximum SOC is calculated.
3. Fifty cycles are performed between the calculated voltages (due to the high degradation of the coin-cells, see Fig. 3 and, for each cycle, the respective specific capacity (mAh/g) is calculated from which the state of health is obtained as:

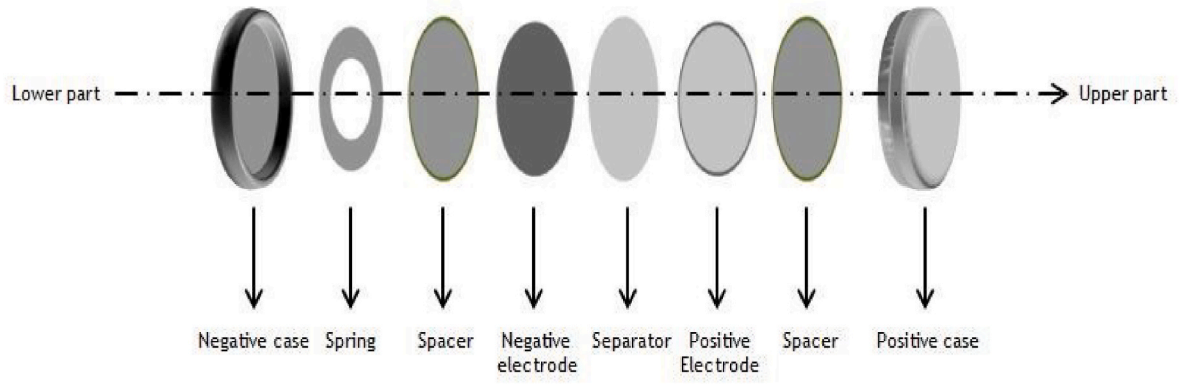

Fig. 1. Coin-cell assembly.

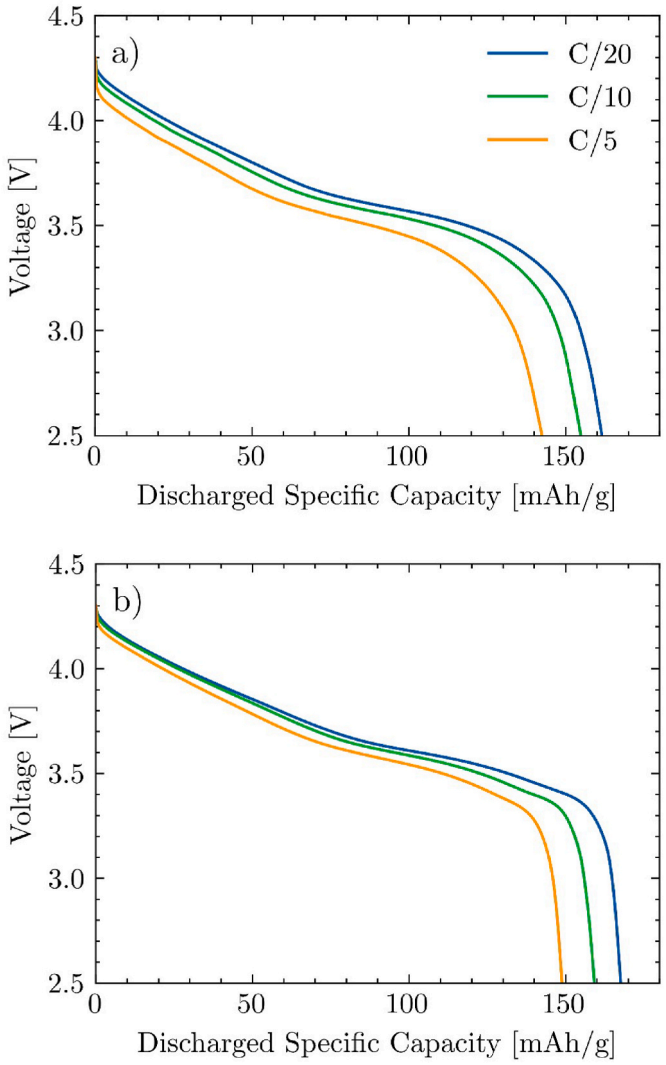

Fig. 2. a) Mean discharge curves of 26 °C tests. b) Mean discharge curves of 45 °C test.

$$\text{SOH}\ (\%) = \frac{\text{Specific capacity at cycle n}}{\text{Initial specific capacity}} \cdot 100 \quad (1)$$

It was decided to analyse the degradation of two different coin cells undergoing cyclic ageing with two different depths of discharge (DOD). The latter has an important influence on SOH during cyclic ageing, along

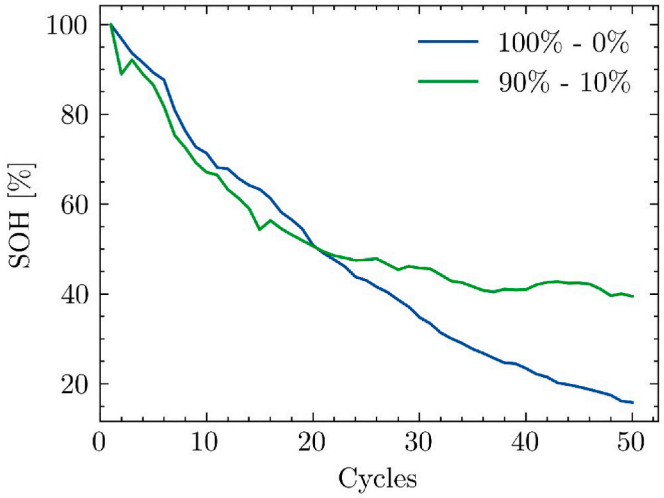

Fig. 3. Capacity degradation in cycle ageing tests with different depths of discharge.

with discharge and charge current and operating temperature [32]. From Fig. 3, it is interesting to highlight the impact of different depths of discharge on the SOH of coin cells: a higher DOD implies a higher degradation rate. This result is in line with what was expected and has been obtained in other work in the literature [33,34]. Indeed, the 100 %–0 % case entails more significant mechanical and chemical stress on the electrodes, which undergo larger volumetric changes, leading to microcracking and a greater loss of active material during cycling compared to the 90 %–10 % case. Although the experimental degradation trend observed in this study does not fully represent that of a commercial battery, which would typically exhibit a more linear decline and reach thousands of cycles [35,36], it is important to note that similar nonlinear degradation patterns have been documented in the literature. For instance, some studies have reported a square root-like decline in capacity over time [37], which aligns more closely with the trend shown in Fig. 6. The choice of using coin cells, despite their faster degradation compared to commercial batteries, was driven by practical considerations related to timing. Laboratory-assembled coin cell, due to their smaller capacity and simpler design compared to full-scale commercial cells, degraded more rapidly allowing for quicker data acquisition and analysis. Coin cells can reach end-of-life in a matter of weeks rather than the several months typically required by commercial-scale cycle-aging tests. For instance, a cycle-aging study on commercial cells might last anywhere from 6 to 12 months (or even longer) [38,39]. The goal was not to replicate the exact lifespan of a commercial battery, but rather to develop and validate a methodology for constructing a digital twin

capable of accurately modelling degradation phenomena. As such, the accelerated degradation in coin cells does not detract from the validity of the methodology or the overall trend of discharge, as it remains consistent with the objectives of this study. Furthermore, the internal material parameters of the coin cells are well-known, enabling the model to produce more accurate results.

2.4. Model creation

The virtual twin calibration procedure can be divided into two parts: a static calibration and a dynamic calibration which will be explored in section 2.5. In this section, the creation of the model for the calibration process will be discussed. The model created in GT-AutoLion (Illinois, USA) is shown in Fig. 4.

- **Battery block:** The first very important thing to include in the battery block is its geometry. Subsequently, the active materials that make up the anode and the cathode must be chosen, in the case under study respectively Graphite and NMC622. The mass fractions of active material are known from previous studies carried out on the materials used for the coin cells and are worth 90 % for graphite and 95 % for NMC622. Next, the assembly details need to be completed by specifying the materials for the electrodes (copper for the anode, aluminium for the cathode), the separator, and the electrolyte. Lastly, it is possible to incorporate a thermal model to account for internal heat generation and heat exchange with the external environment. However, in this study, thermal effects were considered negligible due to the use of low currents, and the temperature of the coin cells was either measured or controlled during the experimental tests.
- **Event Manager:** This block has the function of replicating the experimental tests, controlling the current applied to the battery block to accurately simulate the characterization and cycle aging tests. GT-AutoLion automatically terminates the simulation when the voltage of the experimental curve or the simulated one drops below the cut-off value, settled to 2.5 V.
- **Monitor:** This block is designed to compare experimental and simulated data by plotting voltage versus specific capacity. The simulated voltage is taken directly from the battery model, while the specific capacity is calculated as the integral of the current (preset for various C-rates) and normalized by the mass of active material (NMC622), yielding the specific capacity in mAh/g. Given that the coin cells used in the experiments had slight variations in the mass of active material (within a few milligrams), the mass of NMC622 for the model was assumed to be the average across all cells tested, both at 26 °C and 45 °C. This average value, 31.4 mg, was used to derive the simulated discharge curves. The experimental data, on the other hand, were imported from a pre-defined dataset.
- **Mathematical blocks:** These blocks are employed to calculate the squared differences between the experimental and simulated curves, followed by time integration to obtain the root mean square (RMS) error. The RMS error serves as the objective function to be minimized through case sweep optimization. This optimization is conducted using GT-AutoLion's "Design Optimizer" tool, which aims to identify the best-fit solution that ensures optimal alignment between the experimental and simulated data. The comparison is made across all test conditions, including C/20, C/10, and C/5 discharge curves at 26 °C and 45 °C.

$$\text{Minimize}\left(\text{RMS}=\sqrt{\frac{1}{t}\int_0^t \left(V_{exp}-V_{sim}\right)^2 dt}\right) \tag{2}$$

2.5. Model calibration overview

The process of creating the digital twin can be summarized in the flowchart shown in Fig. 5.

The methodology involves an initial phase dedicated to calibrating static and dynamic phenomena, followed by a subsequent phase focused on degradation phenomena. The first phase thus consists of two main parts:

1. **Static calibration:** In this process, the calibration focuses on the curve obtained at the lowest current rate (C/20), targeting the battery's characteristic parameters that are independent of the current. This approach operates under the assumption that the battery remains in a state of open-circuit voltage (OCV) throughout the discharge cycle, a method commonly referred to as OCV calibration.
2. **Dynamic calibration:** Where the highest C-RATE curves are used to calibrate those parameters that depend on the current and affect the kinetic, resistive, and diffusive phenomena that occur inside the battery [40].

Both processes are characterized of two others distinct steps. The first is a pre-optimization phase, where a manual sensitivity analysis is conducted to determine the appropriate upper and lower bounds of key parameters affecting cell performance. These boundaries help to

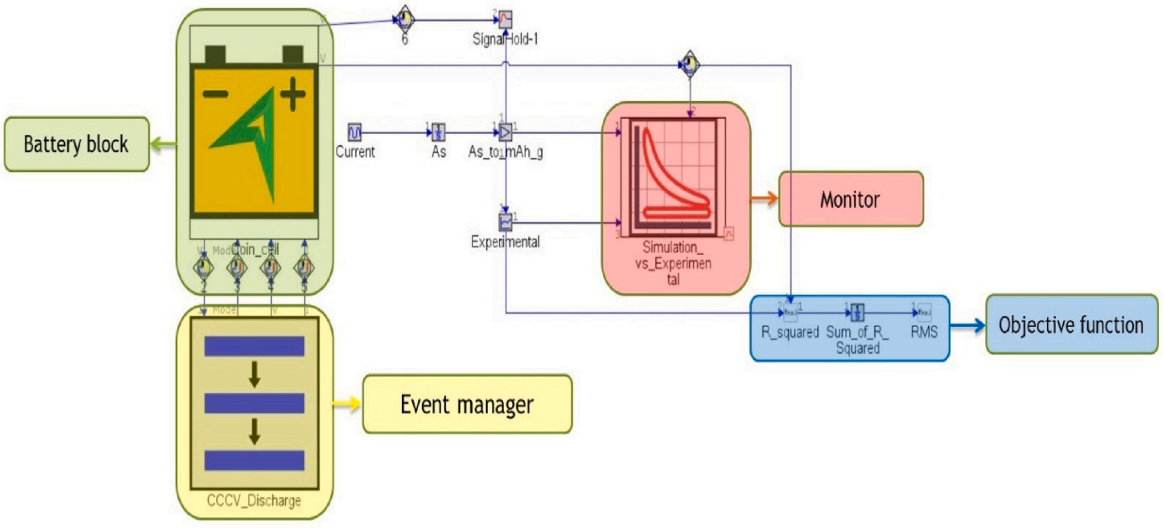

Fig. 4. GT model for static and dynamic characterization.

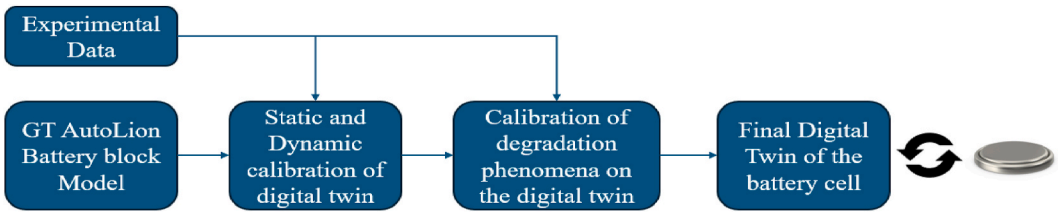

Fig. 5. Methodology overview.

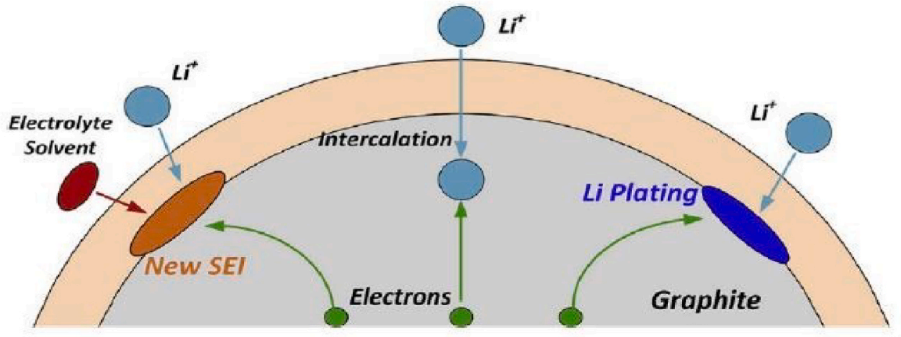

Fig. 6. SEI growth and Lithium plating degradation phenomena [48].

constrain the optimization problem, ensuring that the parameter values remain within realistic limits. The second step involves the actual optimization, where a genetic algorithm is employed. This algorithm iteratively adjusts the parameter values within the predefined bounds to minimize the objective function, which is typically the root mean square error (RMS) between experimental and simulated results. The genetic algorithm uses a multi-objective weighted sum approach to systematically converge on an optimal solution. A constraint is applied during this process, requiring that the simulated discharged capacity remains within ±5 % of the experimental capacity. This constraint ensures that the model maintains realistic performance characteristics. By altering parameter combinations, the genetic algorithm seeks to identify the best set of values that accurately replicate the experimental behaviour of the batteries tested.

For the calibration of degradation phenomena, the overall process mirrors that described for the static and dynamic calibration. The model shown in Fig. 4 was modified to account for the different experimental procedures set in the event manager, and the objective function was updated to include the RMS between the model's state of health (SOH) and the experimentally measured one.

To evaluate the accuracy and good fit of the model, two other post-optimization calculated indices are used [16].

- The Relative Root Mean Square Error (RRMSE) is a metric used to assess model accuracy. A lower value indicates a higher level of precision in the model.

$$RRMSE_X(\%) = \frac{RMS_X}{X_{avg}} \cdot 100 \tag{3}$$

- The R-squared is a goodness of fit index to assess how well the simulated results match the experimental ones. A value close to one indicates a very appropriate fitting.

$$R^2 = 1 - \frac{\sum \left(X_{i,exp} - X_{i,sim}\right)^2}{\sum \left(X_{i,exp} - X_{i,avg}\right)^2} \tag{4}$$

where X can be the Voltage or the SOH.

3. Theory and calculations

3.1. Electrochemical modeling

As already said in the introduction, GT-AutoLion uses the "Pseudo 2D" (P2D) electrochemical model that discretizes the Lithium-ion cell's governing equations using the finite control volume approach. The theoretical formulation of P2D can be deepened in other works in the literature [16,41,42] and the main basics are reported in Appendix A. The battery voltage differs from that of OCV due to some losses called overpotential.

$$V = OCV - V_{act} - V_{ohm} - V_{conc} \tag{5}$$

where:

- V_{act}: It is the activation overpotential that is needed to start the reaction and is the cause of the initial exponential drop. Could be split into two different contributions from the cathode and the anode whose weight depends on the chemistry considered.
- V_{ohm}: It is the ohmic overpotential due to the diffusion of ions through the battery, it is, therefore, a resistive loss and is the cause of the linear voltage drop.
- V_{conc}: It is the concentration overpotential, it appears when the battery is close to its nominal capacity and is due to the low concentration of ions near the electrode (now almost all migrated to the cathode) which takes longer to react leading to another exponential voltage drop. It is a mass transport limitation and so the diffusive phenomena control this loss.

These losses can be calibrated in the electrochemical model, acting on some parameters that describe the behaviour of the battery. The activation (or kinetic) overpotential is described by the Butler – Volmer equation (equation (6)) that correlates the electric current circulating in an electrochemical cell with the cell potential in the case in which the electrode reactions are controlled by the process of transfer of electric charge to the electrodes and not by the transfer of mass between the electrode surfaces and the bulk of the electrolyte.

$$j^{Li} = a_s i_0 \left\{ \exp\left[\frac{\alpha_{an} F}{R_u T}\left(\eta - \frac{R_f j^{Li}}{a_s}\right)\right] - \exp\left[\frac{\alpha_{cat} F}{R_u T}\left(\eta - \frac{R_f j^{Li}}{a_s}\right)\right]\right\} \quad (6)$$

Where a_s is the interfacial area between the two phases, i_0 is the exchange current density, α_{an} and α_{cat} the charge transfer coefficient, R_f the SEI film resistance, η the overvoltage, F the Faraday's constant and R_u the universal ideal gas constant. It is important to point out that equation (6) refers to anode or cathode half-reaction. Following the study of Li et al. [43] the activation overpotential could be adjusted through the exchange current density i_0 and depending on the materials used, there may be a limiting electrode in which this parameter is lower.

The ohmic overpotential originates from the migration of ions inside the electrolyte, the resistivity of the current collectors and the electrodes, as well as the contact resistance between the electrodes and the current collectors. The electrode-to-current-collector interface resistance (R_c) is frequently adjusted to optimize the ohmic resistance, aiming for a voltage alignment between simulated and experimental values within the mid-state-of-charge (SOC) range of the voltage curve.

$$V = \Phi_s(x = L_{cell}) - \Phi_s(x = 0) = \frac{R_c}{A} I \quad (7)$$

The last overpotential, that of diffusion,is described by the Fick equation for the solid and liquid phases (see Appendix A, equations (19) and (21)) and is adjustable through the respective diffusion coefficients D_s and D_e [44–46]. In most cases, the effect of the diffusivity of the solid phase (the anode) is the most relevant but the choice depends on the materials used for the electrodes, the electrolyte, and the design of the battery, for example, the diffusivity in the cathode part increase with the Nickel content [47].

3.1.1. Ageing theory

The main degradation phenomena are the growth of the SEI/CEI layer at the anode and cathode, the loss of active material and the plating of lithium. Other works in the literature have developed and analysed the mathematical models underlying the degradation phenomena [48–53], an extract of these studies is reported below and more in detail in Appendix A for completeness.

- Anode SEI layer growth: In a graphitic anode, an SEI layer forms during the formation cycle and grows in subsequent cycling due to the low equilibrium potential of lithiated graphite. Many studies have shown that the reason for this growth is the reaction between ethylene carbonate and lithium ions.

$$2(CH_2O)_2CO + 2e^- + 2Li^+ \Rightarrow (CH_2OCO_2)_2 + C_2H_4\uparrow \quad (8)$$

$$(CH_2O)_2CO + 2e^- + 2Li^+ \Rightarrow Li_2CO_3 + C_2H_4\uparrow \quad (9)$$

From the reaction of ethylene carbonate with lithium ions there is mainly lithium alkyl carbonate ($(CH_2OCO_2Li)_2$) and little formation of lithium carbonate (Li_2CO_3), therefore only equation (8) will be modelled. The SEI layer growth affects also the EC diffusivity and the effective conductivity of the electrolyte increasing the path that the ions must travel.

- Cathode film growth: Most cathode materials have a high equilibrium potential that is beyond the stable window for typical electrolyte solvents. Thus, the lithium-ion intercalation processes are often preceded by the formation of a surface film on the active cathode material surface. For lithium nickel cobalt oxides, the surface film is mainly composed of polycarbonates, LiF, and oxide reduction products. The oxide film growth can be considered to grow from the following reaction, where R is a radical:

$$Li(Ni, Co)O_2 + ROCO_2R' \Rightarrow (Ni, CO) = O_2R + R'OCO_2Li \quad (10)$$

- Cathode/Anode active material isolation: The intercalation and deintercalation of Li in the structure of active materials leads to mechanical stress and induces cracking and structural damage that quickly leads to the loss of active material during cycling. This loss can occur in the anode, in the cathode or both and depends on the structure and materials of the latter.
- Lithium plating: If the potential in a finite volume of the anode falls below zero volts, cycling lithium (Li^+) will react with electrons (e^-) to form lithium metal. This lithium metal is deposited into the anode, lowering the porosity and the active surface area with consequent drops in performance and possible safety accidents. The deposition of lithium on the anode in lithium-ion batteries (LIBs) is closely associated with the charging circumstances, including low temperatures, rapid charging rates, and overcharging. However, it also relies on battery architecture, such as the ratio of anode to cathode and potential manufacturing flaws.

The anode/cathode layers' growth with lithium plating is schematized in Fig. 6.

4. Results and discussion

4.1. Static calibration

The calibration procedure follows the methodology proposed in subsection 2.5, the parameters that are important for the static balance of the battery are listed and explained below.

- Cathode capacity loading ($Loading^{Ca}$) (mAh/cm^2): is the amount of charge per unit area present at the cathode. It is an important parameter for the energy-power balance of the cell and is influenced by the amount of active material. When there is little material in the cathode, the cell will have a large energy storage capacity, but will not allow high C-rates [54]. It was estimated by dividing the charge capacity of the first cycle at C/20 by the area of the NMC622 disk.
- N/P (−): It is the ratio between the capacity loading of the anode and that of the cathode.

$$\frac{N}{P} = \frac{\text{Anode capacity loading (mAh/g)}}{\text{Cathode capacity loading (mAh/g)}} \quad (11)$$

- NMC622 and Graphite first charge capacity (FCCCa and FCCAn) (mAh/g): During the initial formation and first charge and discharge cycles, a certain amount of lithium, or capacity, is lost for the formation of the initial Solid Electrolyte interface (SEI) layer. The first charge capacity is the amount of lithium accepted, either the graphite or NMC 622, during the initial lithiation of the material (first charge) per unit of active material mass. The FCC of NMC622 was estimated by dividing the capacity of the first charge cycle at C/20 by the mass of NMC622 weighted during battery assembly.
- NMC622 and Graphite first discharge capacity (FDC^{Ca} and FDC^{An}) (mAh/g): is the amount of lithium returned in the cathode and anode materials, after initial lithiation per unit of active material mass. The difference between FCC and FDC represents the irreversible capacity of the cathode and anode respectively, so these processes are related to the coulombic efficiency.
- Maximum voltage NMC622 (U^{Ca}_{max})(V): is the maximum open circuit potential of the NMC622 obtained in a half-cell (with Li/Li^+ counter electrode).

The static calibration was performed using the average C/20 discharge curves at 26 °C and 45 °C, assuming constant temperature conditions. The results of the optimization process are summarized in Table 2.

For a clearer representation, the discharge curve results are presented in Fig. 7. Instead of using an average discharge curve, all

Table 2
Starting, boundaries and final values for the static calibration parameters.

Parameter	Unit	Starting value	Boundaries	Final value
$Loading^{Ca}$	mAh/g	3.35	3.15–3.45	3.362
N/P	–	1.3	1.2–1.35	1.344
FCC^{Ca}	mAh/g	180	170–190	175.01
FDC^{Ca}	mAh/g	165	160–170	163.9
FCC^{An}	mAh/g	370	365–375	374.5
FDC^{An}	mAh/g	345	340–350	348.5
U^{Ca}_{max}	V	4.40	4.3–4.45	4.365

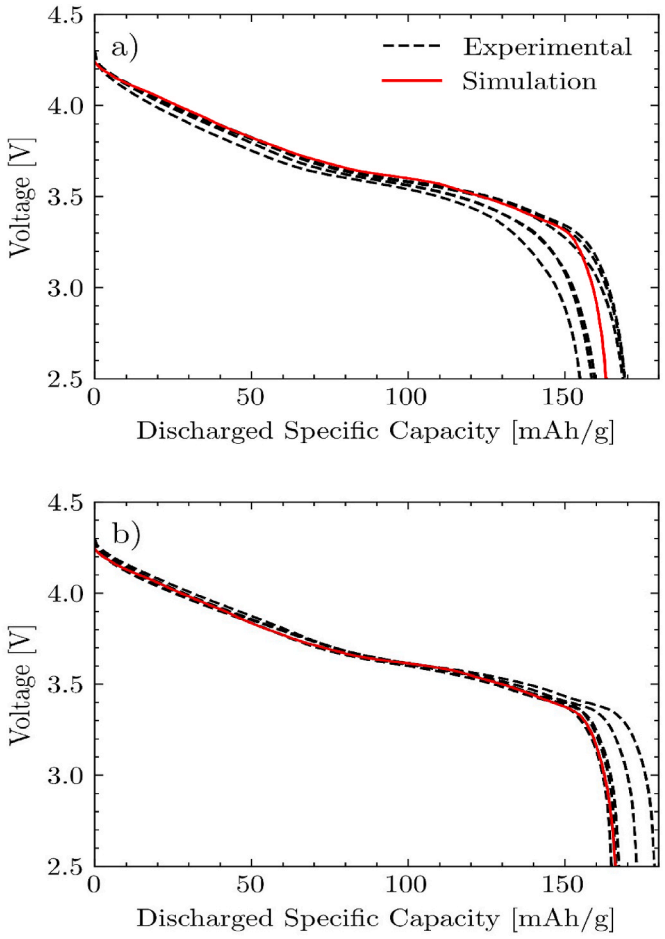

Fig. 7. Simulation discharge curves at C/20 and 26 °C (a), C/20 and 45 °C (b) versus all the experimental curves considered for the calculation of the mean one.

experimental curves from different coin cells were included to provide a more comprehensive comparison with the modelling results. The parameter calibration yielded a good fit for the activation and ohmic regions of the characteristic curve. However, the accuracy in the final diffusion region decreased for the room temperature simulation (Fig. 7a), while it improved for the 45 °C curve (Fig. 7b). It is important to note that the average curve was obtained by discretizing the specific capacity axis and averaging the voltages (i.e., vertically), meaning the simulated discharge curve should not necessarily lie perfectly in the middle of the experimental spread as an indicator of good fitting. Table 3 presents the statistical values used to assess the model performance, confirming that the best precision and fit were achieved for the 45 °C curve.

Table 3
Statistical parameters to evaluate the results of the static calibration.

Case	RRMSE	R^2
C/20 (26 °C)	1.95 %	0.957
C/20 (45 °C)	1.21 %	0.975

The maximum error is 1.95 % in the C/20 case at 26 °C. The discrepancies are since curves at C/20 at 45 °C showed a higher cathode FCC and FDC and a higher capacity loading than the battery at room temperature, leading the optimizer to find a trade-off that penalized the accuracy of the simulation.

4.1.1. Dynamic calibration

After identifying the static parameter sets that define the cell balance, the next step is to calibrate the battery's dynamic behaviour using the higher C-RATE curves. It is essential to introduce the principal parameters that govern the battery's dynamic.

- Cathode exchange current density (i_0) (A/m^2): It appears in the ButlerVolmer equation (equation (6)) and reflects intrinsic rates of electron transfer between an analyte and the electrode providing insights into the structure and bonding. The exchange current density is highly contingent upon the electrode's characteristics, encompassing not just its configuration but also its physical attributes. Moreover, the electroactive species' nature (the analyte) in the solution profoundly influences the exchange current densities, encompassing both its reduced and oxidized states. For example, Lin et al. have reported that MCMB anodes have a performance limit at temperatures < -20 °C compared to the $LiCoO_2$ cathodes [55]. On the contrary, the exchange current density for graphite has been reported in the literature to be greater than the NMC622, respectively 0.8 ÷ 8.4 A/m^2 and 0.1 ÷ 6.0 A/m^2 [42,56–59] For this reason, the cathode was considered limiting, and the respective exchange current density was calibrated. This parameter has a greater influence on the initial drop of the characteristic curve, a lower value of i_0 is reflected in a lower voltage with the same discharge capacity.
- Contact resistance (R_c) (mOhm m^2): is the contact resistance between the electrodes and the collectors, it is a parameter that influences the trend of the curve in the ohmic drop part and is supposed to be the same between cathode-copper and anode-aluminium.
- Graphite Diffusivity (D_{an}) (m^2/s): is the diffusivity of the lithium ions inside the anode electrode, in this case, graphite. As already seen, it appears in the conservation equation of Fick species (in the solid part) and has a great influence on the behaviour of the characteristic curve in the high and low SOC parts.
- NMC622 Diffusivity (D_{ca}) (m^2/s): is the diffusivity of the lithium ions inside the cathode electrode, in this case, NMC622. It is part of the Fick equation applied to the cathode (always in the solid part) and has an influence, albeit secondary to that of graphite [60], on the trend of the characteristic curve in the high and low SOC part.

The starting values of these parameters are those preset by the modelling software. In any case, for i_0, D_{an} and D_{ca} a multiplicative coefficient of the database value is calibrated for which they will have no unit of measurement. Another important parameter on dynamic performance is the heat transfer coefficient h (W/m^{2}K) since as already discussed in the previous sections, the dynamic parameters depend on the temperature. For this study, it was decided to neglect it as the currents involved are small and the temperature is almost constant in both experiments. The dynamic calibration procedure is carried out in the same way as the static one, considering as a case study the average curves at C/10 and C/5 of the tests at 26 °C and 45 °C. The dynamic optimization results are summarized in Table 4.

Fig. 8 shows the simulated discharge curve alongside the experimental curves used to calculate the mean one. A good fit of the experimental curves was obtained in all cases. However, there is a slight difference in the resistance cross-section of the C/5 curve at 45 °C (Fig. 8d). This is because the contact resistance is a function of

Table 4
Starting, boundaries and design value for the dynamic calibration parameters.

Parameter	Unit	Starting value	Boundaries	Final value
pi_0	–	0.3	0.2–0.4	0.299
R_c	mΩ m^2	4.0	2.5–5.5	3.007
pD_{an}	–	0.045	0.03–0.06	0.0444
pD_{ca}	–	0.1	0.03–0.3	0.0508

temperature, which improves performance by reducing the ohmic overpotential (which is increased by the higher current), so the simulation at room temperature will have a greater sensitivity to the variation of this parameter, resulting in convergence towards values that improve the fit of these curves. In any case, this effect is only accentuated by the different trends in this part of the experimental curves, while similar trends are obtained for the diffusive part. The same consideration could be done by seeing the statistical parameters reported in Table 5. The best fitting is obtained for the curve at C/10 at 45 °C with an RRMSE of 0.956 % and R^2 of 0.987. In any case, the fitting and accuracy of the simulations are good for all experimental curves with a maximum RRMSE of 1.29 %.

4.2. Model calibration and validation on cycle ageing tests

The degradation mechanism discussed in section 3.1.1 always leads to a loss of battery capacity during various operating states:

- The electrode film growth model leads to a loss of capacity even when the cell is in storage.
- The loss of active material model leads to a loss of capacity when current passes through the cell.
- The lithium plating model leads to a loss of capacity only in periods of recharging at high currents or recharging at low temperatures.

Being that some phenomena occur both under load and in storage the best experimental procedure will be to pre-calibrate the growth of the anode and cathode layers using calendar ageing tests, where the battery is stored and the loss of capacity over time is monitored. Subsequently, cycle ageing tests are necessary to monitor the loss of capacity during charge and discharge cycles, preferably done at different temperatures, thus obtaining a good estimation of the weight of each single degradation mechanism. Not having calendar ageing tests, an approach will be proposed where the model will be calibrated on the experimental results of cycle ageing considering the effects of the growth of the anode and cathode films (SEI/CEI layers), the loss of anode and cathodic active material (AMI) and the consequent degradation of the diffusivity of the electrolyte (EC). Lithium plating, being that recharging occurs at currents of the order of C/10 and ambient temperature, will be not considered [61,62]. In any case, if calibration were desired, the approach would be the same as that proposed for other degradation mechanisms. The theory behind the modelling of the ageing mechanism is discussed in the previous chapter and Appendix A. In GT-AutoLion, their impact on capacity losses during cycling has been calibrated

Table 5
Statistical parameters to evaluate the results of the dynamic calibration.

Case	RRMSE	R^2
C/10 (26 °C)	1.20 %	0.982
C/10 (45 °C)	0.959 %	0.987
C/5 (26 °C)	1.29 %	0.980
C/5 (45 °C)	1.29 %	0.974

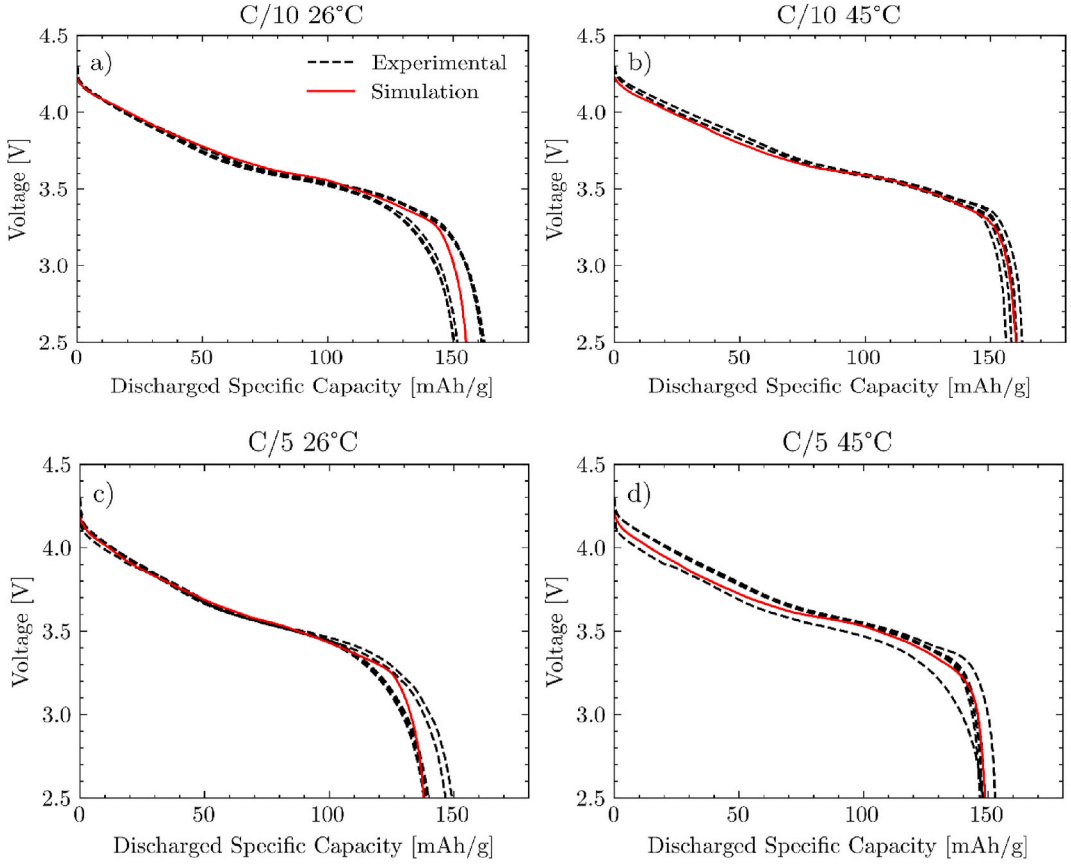

Fig. 8. Simulation discharge curves at C/10 and 26 °C (a), C/10 and 45 °C (b), C/5 and 26 °C (c), C/5 and 45 °C (d) versus all experimental curves considered for the calculation of the mean one.

using Equation (12).

$$\psi = \psi_{ref} \exp\left[\frac{E_{act}}{R}\left(\frac{1}{T_{ref}} - \frac{1}{T}\right)\right] \quad (12)$$

ψ is a generic degradation phenomenon and the pre-exponential part (ψ_{ref}) and the activation energy (E_{act}) are the parameters selected for the calibration process. The optimization steps adhere to the same principles as the static and dynamic calibration and the event manager (Fig. 4) has been modified to perfectly replicate the experimental procedure for cycle ageing described earlier. The results of the optimization process are shown in Table 6 together with the upper and lower boundary conditions.

The optimization intervals are very wide because it is not easy to pre-calibrate the degradation phenomena by considering them together, as a decrease in one could lead to an increase in the interval of another. This aspect could be improved by using calendar ageing tests. In any case, the results of the optimization are best represented in Fig. 9 with the same statistical indices used for the characterization shown in Table 7.

In the 90 %–10 % experimental data case, a better fit is achieved, while the 100 %–0 % case, although presenting a poorer fit, remains acceptable as it reflects the same trend. This difference can be attributed to the manually assembled batteries in both degradation tests, which may introduce random errors in the construction process and complicate cross-validation. The genetic algorithm used for optimization prioritized convergence with the 90 %–10 % experimental data, but the consistency in trends between the two cases is noteworthy. Moreover, these results demonstrate how this procedure coupled with the P2D model can effectively describe degradation processes, including non-linear degradation trends, even with limited experimental data and non-commercial batteries. By enhancing parametric analysis and experimental testing, percentage errors can be reduced, reinforcing the acceptability of the 90 %–10 % case studies.

5. Conclusions

The objective of this study was to develop a digital twin for a lithium-ion coin cell battery (Graphite-NMC622) that accurately replicates the average discharge behaviour of various laboratory-tested batteries and characterizes degradation phenomena through cyclic ageing experiments. This work is especially relevant given the expected rise in electric vehicles and, consequently, lithium-ion battery demand during the energy and transportation transition. Experimental characterization successfully defined the minimum requirements for virtual battery modelling, with tests run up to a C/5 current to optimize coin cell performance. Degradation behaviours were experimentally characterized via cycle ageing tests at two SOC ranges (100 %–0 % and 90 %–10 %), providing a solid foundation for modelling degradation trends. Additional calendar ageing tests at varying temperatures could further enhance degradation modelling by capturing no-load phenomena like SEI/CEI layer growth—an approach we plan to combine with our cycle ageing protocol in future studies. Although these tests would require extensive and time-consuming experimental efforts, they could further reduce the risk of converging on local rather than global minima during the calibration process, thereby improving the accuracy of the digital twin.

Despite these constraints, the virtual coin cell model developed using GT-AutoLion demonstrated excellent accuracy, with an RRMSE lower than 2.0 % and an R^2 higher than 0.95, confirming its capability to simulate degradation trends effectively with limited data. However, further validations are needed to confirm the model's accuracy in modelling battery voltage, particularly under dynamic conditions. As a next step in our research, we plan to evaluate its performance across a broader range of load profiles and operational environments, such as rapid current transients, temperature fluctuations, and varying states of charge to ascertain its robustness. Real-world testing, including representative drive cycles or extended cycling protocols, will provide deeper insights into how the model behaves during transient events and cumulative degradation over time.

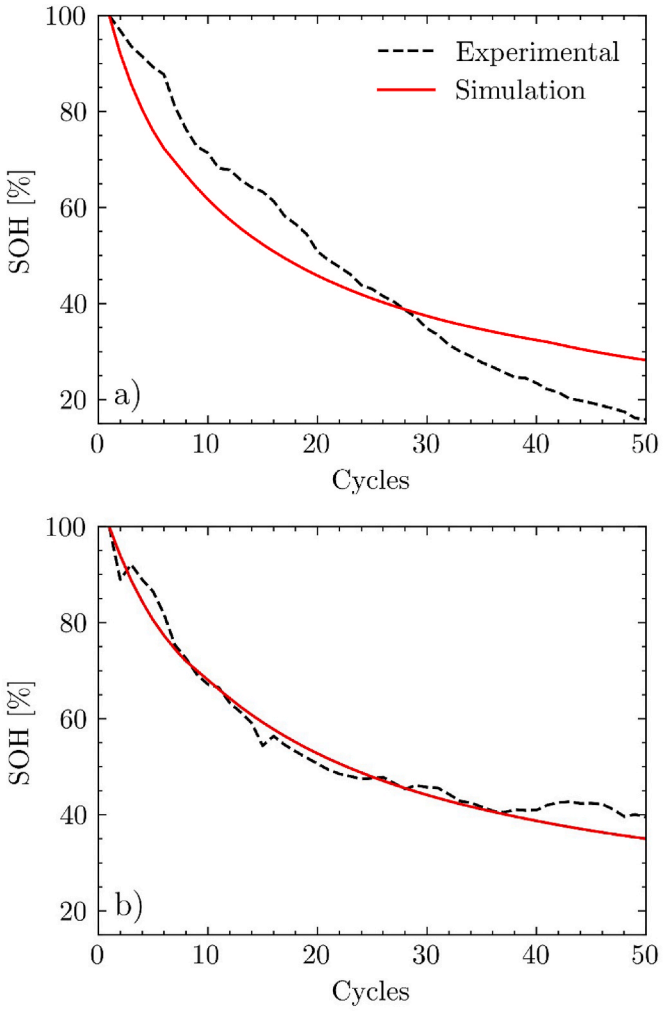

Fig. 9. Results of the calibration of cycle ageing between SOC 100 % and 0 % (a) and 90 %–10 % (b).

Table 6
Starting, boundaries and final values for the cycle ageing calibration parameters.

Parameter	Unit	Starting value	Boundaries	Final value
ψSEI	–	$1e^{-13}$	$1e^{-15}$–$1e^{-10}$	$1.32e^{-12}$
ESEI	*J/mol*	$3e^{5}$	$1e^{4}$–$1e^{6}$	$3.13e^{5}$
ψCEI	–	$1e^{-13}$	$1e^{-15}$–$1e^{-10}$	$2.40e^{-14}$
ECEI	*J/mol*	$3e^{5}$	$1e^{4}$–$1e^{6}$	$7.60e^{5}$
ψEC,An	–	$1e^{-13}$	$1e^{-15}$–$1e^{-10}$	$1e^{-13}$
EEC,An	*J/mol*	$3e^{5}$	$1e^{4}$–$1e^{6}$	$6.12e^{5}$
ψEC,Ca	–	$1e^{-12}$	$1e^{-15}$–$1e^{-10}$	$1e^{-12}$
EEC,Ca	*J/mol*	$1e^{4}$	$1e^{3}$–$1e^{6}$	$1e^{4}$
ψAMI,An	–	$1e^{-13}$	$1e^{-14}$–$1e^{-11}$	$1e^{-13}$
EAMI,An	*J/mol*	$3e^{5}$	$1e^{4}$–$1e^{6}$	$6.45e^{5}$
ψAMI,Ca	–	$1e^{-12}$	$1e^{-15}$–$1e^{-11}$	$6.70e^{-13}$
EAMI,Ca	*J/mol*	$1e^{4}$	$1e^{3}$–$1e^{6}$	$2.69e^{5}$

Table 7
Statistical parameters to evaluate the results of the cycle ageing calibration.

Case	RRMSE	R^2
100 %–0 %	18.4 %	0.882
90 %–10 %	5.64 %	0.969

This methodology can be easily applied to different battery chemistries, as only the parameters in the P2D model equations need to be adjusted, and GT-AutoLion is equipped with a wide range of material options. Moreover, it can also be scaled to battery packs whose series-parallel arrangement is known. Each cell can be represented individually by the developed digital model, as also demonstrated by Astaneh et al. [16] in their work on modelling a battery pack for mining applications. In this way, the battery pack can be discretized into several modules, where each module is treated as a lumped model. The successful validation of the characterization procedure for creating this digital twin paves the way for many valuable applications. With this digital twin model, companies can not only optimize battery design by analysing the impact of critical parameters on performance but also leverage it to enhance the overall Battery Management System (BMS). By doing so, companies can implement advanced usage modes that help preserve battery health, extend overall life cycles, and maintain stable performance across various operating conditions. This approach is exemplified by the work of Biju et al. [63], who employed GT-AutoLion to accurately predict both SOC and SOH. By providing deeper insights into battery behaviour, the model helps refine cell and pack configurations for greater power density, increased energy capacity, and improved longevity. In turn, this can drive more effective charging and discharging protocols, inform thermal management strategies, and support real-time decision-making, ultimately increasing battery safety, reliability, and operating efficiency.

Furthermore, GT-AutoLion's digital twin can be integrated with other subsystems (such as temperature control) or incorporated into complete electric vehicle simulations. This enables stakeholders to verify the proper sizing and performance of components and continuously optimize the powertrain. For example, Vijay et al. [64], utilized GT-AutoLion's gas venting and thermal runaway modelling capabilities to investigate different cooling concepts for a battery pack. Overall, this framework provides a versatile tool for developing cost-effective, high-performance, and sustainable battery solutions for applications spanning from automotive to large-scale energy storage systems.

The author(s) declare(s) that there are no conflicts of interest regarding the publication of this paper.

CRediT authorship contribution statement

Francesco Mazzeo: Writing – original draft, Validation, Software, Methodology, Investigation, Formal analysis, Data curation, Conceptualization. **Eduardo Graziano:** Supervision, Software. **Silvia Bodoardo:** Supervision. **Davide Papurello:** Writing – review & editing, Writing – original draft, Validation, Supervision, Methodology, Investigation, Formal analysis, Data curation, Conceptualization.

Declaration of competing interest

The authors declare that they have no known competing financial interests or personal relationships that could have appeared to influence the work reported in this paper.

Acknowledgements

The work presented in this article derives from the work developed by the first author, Francesco Mazzeo, and presented as an Energy Engineering thesis at the Polytechnic University of Turin.

Appendix A

In the P2D model, the Cathode, Separator, and Anode are discretized in the "thickness" direction. In every finite control volume within the Cathode and Separator, there exists a single spherical depiction of active material, each discretized into uniform volumes along the radial direction. The electrode is considered a superposition of two phases, a solid electrode phase and an electrolyte phase. At the interface of these two phases, the electrochemical reaction takes place. The potential of these two phases (solid Φ_s and liquid Φ_e) can be described using the law of conservation of charge, in particular, Ohm's law becomes respectively:

- Solid phase:

$$\frac{\partial}{\partial x}\left(\sigma_s^{eff}\frac{\partial \Phi_s}{\partial x}\right) - j^{Li} - a_{dl}C\frac{\partial(\Phi_s - \Phi_e)}{\partial t} = 0 \tag{13}$$

Where σ_s^{eff} is the effective conductivity in solid phase, j^{Li} is the volumetric intercalation current, a_{dl} is the electric double layer area, C is the electric double layer capacitance. At the electrode/current collector interface, the boundary condition for the charge flux is:

$$BCs: -\sigma_s^{eff}\left[\frac{\partial \Phi_s}{\partial x}\right]_{x=0} = -\sigma_s^{eff}\left[\frac{\partial \Phi_s}{\partial x}\right]_{x=L_{an}+L_{sep}+L_{cat}} = \frac{I}{A} \tag{14}$$

While at the electrode/separator interface there isn't charge flux:

$$BCs: \left[\frac{\partial \Phi_s}{\partial x}\right]_{x=L_{an}} = \left[\frac{\partial \Phi_s}{\partial x}\right]_{x=L_{an}+L_{sep}} = 0 \tag{15}$$

- Liquid electrolyte phase:

$$\frac{\partial}{\partial x}\left(k^{eff}\frac{\partial \Phi_s}{\partial x}\right) + \frac{\partial}{\partial x}\left(k_d^{eff}\frac{\partial \ln(c_e)}{\partial x}\right) + j^{Li} + a_{dl}C\frac{\partial(\Phi_s - \Phi_e)}{\partial x} = 0 \tag{16}$$

Where c_e is the concentration of lithium in the electrolyte phase. A zero potential variation boundary condition can be used at the electrode/current collector interfaces:

$$\text{BCs}: \left[\frac{\partial \Phi_e}{\partial x}\right]_{x=0} = \left[\frac{\partial \Phi_e}{\partial x}\right]_{x=L_{an}+L_{sep}+L_{cat}} = 0 \tag{17}$$

In equations (13) and (16), The reaction current density and the double-layer capacitance manifest with opposing signs to ensure electroneutrality both locally and globally. The electrical double layer (EDL) forms on the surface of an object upon exposure to a fluid. The EDL consists of two parallel layers of charge enveloping the object. The first layer, known as the surface charge, comprises ions adsorbed onto the object due to chemical interactions while the second one consists of ions attracted to the surface charge by the Coulomb force. This second layer is loosely associated with the object and consists of free ions that move within the fluid due to electric attraction and thermal motion rather than being firmly anchored. It is thus referred to as the "diffuse layer". Since it is schematized as a series of two capacitors, the dynamic effect on the potential of the two phases occurs mainly in the case of current pulses of the order of milliseconds, otherwise it is negligible (as in this study). The effective diffusional conductivity (k_d^{eff}) is described by concentrated solution theory:

$$k_d^{eff} = \frac{2R_u T k^{eff}}{F}\left(t_+^0 - 1\right)\left(1 + \frac{d\ln(f_\pm)}{d\ln(c_e)}\right) \tag{18}$$

Where R_u is the universal gas costant, T is the tempearture, k^{eff} is the effective ionic conductivity, F the Faraday's costant, t_+^0 the initial transfer number and $f_\pm$ the average ionic activity coefficient.

As the lithium-ion concentration changes the intercalation/deintercalation processes within the solid phase, it is necessary to apply a mass conservation law inside the cell through Fick's second law. The distribution of Li in the spherical particles located in each control volume of the electrodes is predicted as:

- Solid phase:

$$\frac{\partial c_s}{\partial t} = \frac{1}{r^2}\frac{\partial}{\partial r}\left(D_s r^2 \frac{\partial c_s}{\partial r}\right) \tag{19}$$

Where c_s is the lithium concentration in solid phase and D_s the diffusional coefficient of lithium in solid phase. No species source exists at the centre of the electrode particles, hence the boundary condition is defined as follows:

$$\text{BCs}: \left[\frac{\partial c_s}{\partial r}\right]_{r=0} = 0; \; -D_s\left[\frac{\partial c_s}{\partial r}\right]_{r=R_s} = \frac{j^{Li}}{a_s F} \tag{20}$$

Liquid electrolyte phase:

$$\frac{\partial(\epsilon_e c_e)}{\partial t} = \frac{\partial}{\partial x}\left(D_e \frac{\partial c_e}{\partial x}\right) + \frac{1 - t_+^0}{F} j^{Li} \tag{21}$$

Where ϵ_e is the electrode porosity, D_e the diffusion coefficient of lithium in electrolyte phase. Lithium cannot diffuse through the current collectors, as set by the following boundary condition:

$$\text{BCs}: \left[\frac{\partial c_e}{\partial x}\right]_{x=0} = \left[\frac{\partial c_e}{\partial x}\right]_{x=L_{an}+L_{sep}+L_{cat}} = 0 \tag{22}$$

At the interface of the solid and liquid phases, the electrochemical reaction takes place. This reaction is described by the Butler-Volmer equation that expresses the volumetric intercalation reaction current of Li in the given electrode as:

$$j^{Li} = a_s i_0 \left\{ \exp\left[\frac{\alpha_{an} F}{R_u T}\left(\eta - \frac{R_f j^{Li}}{a_s}\right)\right] - \exp\left[\frac{\alpha_{cat} F}{R_u T}\left(\eta - \frac{R_f j^{Li}}{a_s}\right)\right]\right\} \tag{23}$$

Where i_0 is the exchange current density, α_{an} and α_{cat} the charge transfer coefficient, R_f the SEI film resistance, η the overvoltage and a_s is the interfacial area between the two phases, calculated considering the solid phase as a sequence of spheres:

$$a_s = \frac{3\epsilon_s}{r_p} = \frac{1 - \epsilon_e - \epsilon_f}{r_p} \tag{24}$$

where ϵ_f is the porosity (volume fraction) of the fillers. η is defined as the difference between the solid and liquid phase potentials, minus the open-circuit potential of the solid, that is $\eta = \Phi_s - \Phi_e - U$. R_f is the electronic resistance of the surface film layer at the negative and positive electrodes. While the exchange current density of the intercalation reaction (based on reaction surface area) i_0, exhibits modest dependency on electrolyte and solid surface concentrations.

The partial differential equations (13) and (16),19,21 are integrated through the intercalation current density (j^{Li}) via the Butler-Volmer equation which defines cell electrochemical kinetics.

From equation (8), 2 mol of Li^+ and 2 mol of electrons are being consumed, which reduces the columbic efficiency of the system with the following kinetic equations:

$$j_{SEI} = a_s i_{o,SEI}\left\{\exp\left[\frac{\alpha_{c,SEI} F}{R_u T}\left(\Phi_s - \Phi_e - U_{SEI} - \frac{R_{SEI} j^{Li}}{a_s}\right)\right]\right\} \tag{25}$$

Where j_{SEI} is the side reaction current density (based on reaction surface area, U_{SEI} is the equilibrium potential for the first chemical reaction, j^{Li} is the total current density and R_{SEI} is the resistance of the SEI layer. The exchange current density of the side reaction ($i_{0,SEI}$) depends on EC concentration at the reaction surface. Due to the creation of a side reaction at the interface of the active material particle and the SEI layer, the bulk EC (c_{EC}) has to diffuse through the porous SEI layer to reach the reaction site, and Fick's law for the EC diffusion can be written:

$$\frac{\partial c_{EC}}{\partial t} = D_{EC}^{eff}\frac{\partial^2 c_{EC}}{\partial r^2} \tag{26}$$

The EC effective diffusivity accounts for the torturous path in the SEI and is related to SEI layer porosity (ϵ_{SEI}) and EC diffusivity in the bulk solution (D_{EC}) by the following Bruggeman relationship, where n is the Bruggeman exponent:

$$D_{EC}^{eff} = D_{EC}(\epsilon_{SEI})^n \tag{27}$$

By solving the above equations, the growth rate of the SEI layer thickness (λ_{SEI}) can be calculated as:

$$\frac{\partial \lambda_{SEI}}{\partial x} = -\frac{i_{s,A} M_{SEI}}{2F\rho_{SEI}} \tag{28}$$

Where M_{SEI} and ρ_{SEI} are the molecular weight and density of the SEI layer, respectively. The resistance of the SEI layer can be calculated by:

$$R_{SEI} = \frac{\lambda_{SEI}}{k_{SEI}^{eff}} \tag{29}$$

k_{SEI}^{eff} is the effective conductivity of the electrolyte through the porous SEI layer, also this parameter, like the effective diffusivity of the EC, is related to the inherent conductivity of the electrolyte (k_{SEI}) via the standard Bruggeman relationship:

$$k_{SEI}^{eff} = k_{SEI}(\epsilon_{SEI})^n \tag{30}$$

For the cathode film growth, GT AutoLion models the oxide film formation and growth in the cathode by using the following rate equation:

$$J_{s,C} = k_{s,C} C_{EC,s} C_{Li_x(Ni,CO)O_2} \tag{31}$$

Here, $J_{s,C}$ is the side reaction rate per surface area, $k_{s,C}$ is the reaction rate coefficient, $C_{EC,s}$ is the EC concentration at the surface of the active material particle, and $C_{Lix(Ni,CO)O2}$ is the cathode material molar concentration. The loss of active cathode material due to the above reaction is given by:

$$\frac{\partial \epsilon_{Li_x(Ni,Co)O_2}}{\partial x} = -\frac{a_s J_{s,C}}{C_{Li_x(Ni,Co)O_2}} \tag{32}$$

$\epsilon_{Li(Ni,Co)O2}$, is the active material volume fraction in the electrode. This loss of active material in the cathode leads to capacity fade. As for the SEI layer, the growth of the cathode film is modelled with a mass balance:

$$\frac{\partial \lambda_{film}}{\partial t} = J_{s,C}\frac{M_{film}}{\rho_{film}} \tag{33}$$

where, again, ρ_{film} represents the cathode oxide film growth, M_{film} represents the molecular weight of the film, and ρ_{film} represents the density of the film.

The active material isolation (AMI) is a consequence of the lithium intercalation process, it is possible to relate the isolation rate to the intercalation current such that:

$$\frac{\partial \epsilon_{AM}}{\partial t} = -k(T)\left|j^{Li}\right| \tag{34}$$

where ϵ_{AM} is the volume fraction of active material, k(T) is a temperature-dependent fitting parameter, and j^{Li} is always the intercalation current.

In GT-AutoLion the Lithium plating is taken into account together with the growth of the SEI layer:

$$\frac{\partial \epsilon}{\partial t} = -a_s\frac{d(\lambda_{SEI} + \lambda_{Lip})}{dt} \tag{35}$$

where ϵ represents porosity, a_s represents the volume-specific reaction surface area, and $\lambda_{SEI} + \lambda_{Lip}$ represents the growth of the surface film thickness. As the side reaction proceeds, there is a decrease in the available active surface area of the negative electrode because of the clogging of the particle surface due to the side reaction product, which is represented by:

$$a_s = -a_{s,0}\left[1 - \left(\frac{\epsilon_0 - \epsilon}{\epsilon_0}\right)\zeta\right] \tag{36}$$

where ζ is the morphology factor of the side reaction product. Its value is between 0 and 1 and a $\zeta = 0$ means that the side reaction products instantaneously spread over the whole reaction surface and block the reaction completely. While $\zeta = 1$, means that the side reaction products spread over the reaction surface laterally.

References

[1] M. Kovačić, M. Mutavdžija, K. Buntak, New paradigm of sustainable urban mobility: electric and autonomous vehicles—a review and bibliometric analysis, Sustainability 14 (15) (Jan. 2022), https://doi.org/10.3390/su14159525. Art. no. 15.

[2] F. Mazzeo, L. Di Napoli, and M. Carello, 'Assessing Open Circuit Voltage Losses in PEMFCs: A New Methodological Approach', Energies, vol. 17, no. 2785 doi: https://doi.org/10.3390/en17112785.

[3] D. F. Birol, 'Key World Energy Statistics 2021'.

[4] M. Carello, H. de Carvalho Pinheiro, L. Longega, L. Di Napoli, Design and Modelling of the Powertrain of a Hybrid Fuel Cell Electric Vehicle, vol. 3, 2021, https://doi.org/10.4271/2021-01-0734.

[5] Comité Technique/Technical Committee/Comité Técnico 2020-2023 4.4 Tunnels/Tunnels/Túneles, 'Impact of New Propulsion Technologies on Road Tunnel Operations and Safety - Literature Review, PIARC, 2022 [Online]. Available: https://www.piarc.org/en/order-library/37387-en-ImpactofNewPropulsionTechnologiesonRoadTunnelOperationsandSafety-Literaturereview. (Accessed 3 November 2023).

[6] W. Zhang, X. Fang, C. Sun, The alternative path for fossil oil: electric vehicles or hydrogen fuel cell vehicles? J. Environ. Manag. 341 (Sep. 2023) 118019 https://doi.org/10.1016/j.jenvman.2023.118019.

[7] Shares of EV sales by scenario, 2021-2030 – Charts – Data & Statistics, IEA Accessed: November. 6, 2024. [Online]. Available: https://www.iea.org/data-and-statistics/charts/shares-of-ev-sales-by-scenario-2021-2030.

[8] S. Chavan, et al., Thermal runaway and mitigation strategies for electric vehicle lithium-ion batteries using battery cooling approach: a review of the current status and challenges, J. Energy Storage 72 (Nov. 2023) 108569, https://doi.org/10.1016/j.est.2023.108569.

[9] X. Feng, D. Ren, X. He, M. Ouyang, Mitigating thermal runaway of lithium-ion batteries, Joule 4 (4) (Apr. 2020) 743–770, https://doi.org/10.1016/j.joule.2020.02.010.

[10] Y. Yang, R. Wang, Z. Shen, Q. Yu, R. Xiong, W. Shen, Towards a safer lithium-ion batteries: a critical review on cause, characteristics, warning and disposal strategy for thermal runaway, Advances in Applied Energy 11 (Sep. 2023) 100146, https://doi.org/10.1016/j.adapen.2023.100146.

[11] P. Saechan, I. Dhuchakallaya, Numerical study on the air-cooled thermal management of Lithium-ion battery pack for electrical vehicles, Energy Rep. 8 (Apr. 2022) 1264–1270, https://doi.org/10.1016/j.egyr.2021.11.089.

[12] O.E. Rojas, M.A. Khan, A review on electrical and mechanical performance parameters in lithium-ion battery packs, J. Clean. Prod. 378 (Dec. 2022) 134381, https://doi.org/10.1016/j.jclepro.2022.134381.

[13] R. Kumar, V. Goel, A study on thermal management system of lithium-ion batteries for electrical vehicles: a critical review, J. Energy Storage 71 (Nov. 2023) 108025, https://doi.org/10.1016/j.est.2023.108025.

[14] J. Liang, Y. Gan, Y. Li, Investigation on the thermal performance of a battery thermal management system using heat pipe under different ambient temperatures, Energy Convers. Manag. 155 (Jan. 2018) 1–9, https://doi.org/10.1016/j.enconman.2017.10.063.

[15] Comparison of modeling predictions with experimental data from plastic lithium ion cells - IOPscience [Online]. Available: https://iopscience.iop.org/article/10.1149/1.1836921. (Accessed 22 October 2024).

[16] M. Astaneh, et al., Calibration optimization methodology for lithium-ion battery pack model for electric vehicles in mining applications, Energies 13 (14) (Jan. 2020), https://doi.org/10.3390/en13143532. Art. no. 14.

[17] N. Natarajan, A. Panday, S. Duddu, T.T. Singh, D. Kesavan, S. Annabathula, Electrochemical & equivalent circuit modelling and validation of lithium-ion cell in GT-AutoLion. SAE Technical Paper 2022-28–0338, SAE International, Warrendale, PA, Oct. 2022, https://doi.org/10.4271/2022-28-0338.

[18] G. Barletta, P. DiPrima, D. Papurello, Thévenin's battery model parameter estimation based on simulink, Energies 15 (17) (Jan. 2022), https://doi.org/10.3390/en15176207. Art. no. 17.

[19] U. Chopra, N. Biju, Real-world aging prediction of a lithium-ion battery using a simulation-driven approach. SAE Technical Paper 2023-01–0508, SAE International, Warrendale, PA, Apr. 2023, https://doi.org/10.4271/2023-01-0508.

[20] M. Hassini, E. Redondo-Iglesias, P. Venet, Lithium–ion battery data: from production to prediction, Batteries 9 (7) (Jul. 2023), https://doi.org/10.3390/batteries9070385. Art. no. 7.

[21] Y. Li, et al., Model order reduction techniques for physics-based lithium-ion battery management: a survey, IEEE Industrial Electronics Magazine 16 (3) (Sep. 2022) 36–51, https://doi.org/10.1109/MIE.2021.3100318.

[22] S. Katoch, S.S. Chauhan, V. Kumar, A review on genetic algorithm: past, present, and future, Multimed Tools Appl 80 (5) (Feb. 2021) 8091–8126, https://doi.org/10.1007/s11042-020-10139-6.

[23] Y. Ye, Y. Shi, N. Cai, J. Lee, X. He, Electro-thermal modeling and experimental validation for lithium ion battery, J. Power Sources 199 (Feb. 2012) 227–238, https://doi.org/10.1016/j.jpowsour.2011.10.027.

[24] S. Ma, et al., Temperature effect and thermal impact in lithium-ion batteries: a review, Prog. Nat. Sci.: Mater. Int. 28 (6) (Dec. 2018) 653–666, https://doi.org/10.1016/j.pnsc.2018.11.002.

[25] Q. Wang, P. Ping, X. Zhao, G. Chu, J. Sun, C. Chen, Thermal runaway caused fire and explosion of lithium ion battery, J. Power Sources 208 (Jun. 2012) 210–224, https://doi.org/10.1016/j.jpowsour.2012.02.038.

[26] M. Matsumiya, M. Terazono, K. Tokuraku, Temperature dependence of kinetics and diffusion coefficients for ferrocene/ferricenium in ammonium-imide ionic liquids, Electrochim. Acta 51 (7) (Jan. 2006) 1178–1183, https://doi.org/10.1016/j.electacta.2005.06.006.

[27] P. Arora, R.E. White, M. Doyle, Capacity fade mechanisms and side reactions in lithium-ion batteries, J. Electrochem. Soc. 145 (10) (Oct. 1998) 3647, https://doi.org/10.1149/1.1838857.

[28] M. Ochida, et al., Influence of manganese dissolution on the degradation of surface films on edge plane graphite negative-electrodes in lithium-ion batteries, J. Electrochem. Soc. 159 (7) (Jul. 2012) A961, https://doi.org/10.1149/2.031207jes.

[29] C. Vidal, O. Gross, R. Gu, P. Kollmeyer, A. Emadi, xEV Li-ion battery low-temperature effects—review, IEEE Trans. Veh. Technol. 68 (5) (May 2019) 4560–4572, https://doi.org/10.1109/TVT.2019.2906487.

[30] A. Barré, B. Deguilhem, S. Grolleau, M. Gérard, F. Suard, D. Riu, A review on lithium-ion battery ageing mechanisms and estimations for automotive applications, J. Power Sources 241 (Nov. 2013) 680–689, https://doi.org/10.1016/j.jpowsour.2013.05.040.

[31] N. Andrenacci, V. Sglavo, and F. Vellucci, 'Definizione della procedura sperimentale di invecchiamento delle celle litio-ione'.

[32] M. Jafari, K. Khan, L. Gauchia, Deterministic models of Li-ion battery aging: it is a matter of scale, J. Energy Storage 20 (Dec. 2018) 67–77, https://doi.org/10.1016/j.est.2018.09.002.

[33] P. Lall, V. Soni, G. Sethi, K. Yiang, Effect of high and low storage temperatures, storage duration and varying depth of discharge on coin cell SOH degradation, in: 2022 21st IEEE Intersociety Conference on Thermal and Thermomechanical Phenomena in Electronic Systems (iTherm), May 2022, pp. 1–8, https://doi.org/10.1109/iTherm54085.2022.9899574.

[34] State of health prediction model based on internal resistance - ji - 2020 - international journal of energy research - wiley online library [Online]. Available: https://onlinelibrary.wiley.com/doi/abs/10.1002/er.5383. (Accessed 22 October 2024).

[35] S. Liu, et al., Analysis of cyclic aging performance of commercial Li4Ti5O12-based batteries at room temperature, Energy 173 (Apr. 2019) 1041–1053, https://doi.org/10.1016/j.energy.2019.02.150.

[36] X. Han, M. Ouyang, L. Lu, J. Li, Cycle life of commercial lithium-ion batteries with lithium titanium oxide anodes in electric vehicles, Energies 7 (8) (Aug. 2014), https://doi.org/10.3390/en7084895. Art. no. 8.

[37] Y. Li, et al., Evolution of aging mechanisms and performance degradation of lithium-ion battery from moderate to severe capacity loss scenarios, Chem. Eng. J. 498 (Oct. 2024) 155588, https://doi.org/10.1016/j.cej.2024.155588.

[38] M. Naumann, F.B. Spingler, A. Jossen, Analysis and modeling of cycle aging of a commercial LiFePO4/graphite cell, J. Power Sources 451 (Mar. 2020) 227666, https://doi.org/10.1016/j.jpowsour.2019.227666.

[39] K. Jalkanen, J. Karppinen, L. Skogström, T. Laurila, M. Nisula, K. Vuorilehto, Cycle aging of commercial NMC/graphite pouch cells at different temperatures, Appl. Energy 154 (Sep. 2015) 160–172, https://doi.org/10.1016/j.apenergy.2015.04.110.

[40] L. Ménard, G. Fontès, S. Astier, Dynamic energy model of a lithium-ion battery, Math. Comput. Simulat. 81 (2) (Oct. 2010) 327–339, https://doi.org/10.1016/j.matcom.2010.07.026.

[41] E. Hosseinzadeh, J. Marco, P. Jennings, Electrochemical-thermal modelling and optimisation of lithium-ion battery design parameters using analysis of variance, Energies 10 (9) (Sep. 2017), https://doi.org/10.3390/en10091278. Art. no. 9.

[42] Simplified electrochemical and thermal model of LiFePO4-graphite Li-ion batteries for fast charge applications - IOPscience [Online]. Available: https://iopscience.iop.org/article/10.1149/2.064209jes/meta. (Accessed 22 October 2024).

[43] J. Li, L. Zou, F. Tian, X. Dong, Z. Zou, H. Yang, Parameter identification of lithium-ion batteries model to predict discharge behaviors using heuristic algorithm, J. Electrochem. Soc. 163 (8) (Jun. 2016) A1646, https://doi.org/10.1149/2.0861608jes.

[44] S. Santhanagopalan, Q. Guo, R.E. White, Parameter estimation and model discrimination for a lithium-ion cell, J. Electrochem. Soc. 154 (3) (Jan. 2007) A198, https://doi.org/10.1149/1.2422896.

[45] Parameter estimation of an electrochemistry-based lithium-ion battery model using a two-step procedure and a parameter sensitivity analysis - jin - 2018 - international Journal of Energy Research - wiley Online Library [Online]. Available: https://onlinelibrary.wiley.com/doi/full/10.1002/er.4022. (Accessed 22 October 2024).

[46] V. Ramadesigan, K. Chen, N.A. Burns, V. Boovaragavan, R.D. Braatz, V. R. Subramanian, Parameter estimation and capacity fade analysis of lithium-ion batteries using reformulated models, J. Electrochem. Soc. 158 (9) (Jul. 2011) A1048, https://doi.org/10.1149/1.3609926.

[47] M.A. Cabañero, N. Boaretto, M. Röder, J. Müller, J. Kallo, A. Latz, Direct determination of diffusion coefficients in commercial Li-ion batteries, J. Electrochem. Soc. 165 (5) (Mar. 2018) A847, https://doi.org/10.1149/2.0301805jes.

[48] X.-G. Yang, Y. Leng, G. Zhang, S. Ge, C.-Y. Wang, Modeling of lithium plating induced aging of lithium-ion batteries: transition from linear to nonlinear aging, J. Power Sources 360 (Aug. 2017) 28–40, https://doi.org/10.1016/j.jpowsour.2017.05.110.

[49] H. Adenusi, G.A. Chass, S. Passerini, K.V. Tian, G. Chen, Lithium batteries and the solid electrolyte interphase (SEI)—progress and outlook, Adv. Energy Mater. 13 (10) (2023) 2203307, https://doi.org/10.1002/aenm.202203307.

[50] M. Safari, M. Morcrette, A. Teyssot, C. Delacourt, Multimodal physics-based aging model for life prediction of Li-ion batteries, J. Electrochem. Soc. 156 (3) (Dec. 2008) A145, https://doi.org/10.1149/1.3043429.

[51] R. Li, S. O'Kane, M. Marinescu, G.J. Offer, Modelling solvent consumption from SEI layer growth in lithium-ion batteries, J. Electrochem. Soc. 169 (6) (Jun. 2022) 060516, https://doi.org/10.1149/1945-7111/ac6f84.
[52] Crack pattern formation in thin film lithium-ion battery electrodes - IOPscience [Online]. Available: https://iopscience.iop.org/article/10.1149/1.3574027. (Accessed 22 October 2024).
[53] J. Vetter, et al., Ageing mechanisms in lithium-ion batteries, J. Power Sources 147 (1) (Sep. 2005) 269–281, https://doi.org/10.1016/j.jpowsour.2005.01.006.
[54] Y. Kim, et al., Investigation of mass loading of cathode materials for high energy lithium-ion batteries, Electrochem. Commun. 147 (Feb. 2023) 107437, https://doi.org/10.1016/j.elecom.2023.107437.
[55] H. -p Lin, et al., Low-temperature behavior of Li-ion cells, Electrochem. Solid State Lett. 4 (6) (Apr. 2001) A71, https://doi.org/10.1149/1.1368736.
[56] A.M. Colclasure, R.J. Kee, Thermodynamically consistent modeling of elementary electrochemistry in lithium-ion batteries, Electrochim. Acta 55 (28) (Dec. 2010) 8960–8973, https://doi.org/10.1016/j.electacta.2010.08.018.
[57] M. Ecker, T.K.D. Tran, P. Dechent, S. Käbitz, A. Warnecke, D.U. Sauer, Parameterization of a physico-chemical model of a lithium-ion battery: I. Determination of parameters, J. Electrochem. Soc. 162 (9) (Jun. 2015) A1836, https://doi.org/10.1149/2.0551509jes.
[58] P.-C. Tsai, et al., Single-particle measurements of electrochemical kinetics in NMC and NCA cathodes for Li-ion batteries, Energy Environ. Sci. 11 (4) (Apr. 2018) 860–871, https://doi.org/10.1039/C8EE00001H.
[59] O. Chaouachi, J.-M. Réty, S. Génies, M. Chandesris, Y. Bultel, Experimental and theoretical investigation of Li-ion battery active materials properties: application to a graphite/Ni0.6Mn0.2Co0.2O2 system, Electrochim. Acta 366 (Jan. 2021) 137428, https://doi.org/10.1016/j.electacta.2020.137428.
[60] Y. Chen, J. Key, K. O'Regan, T. Song, Y. Han, E. Kendrick, Revealing the rate-limiting electrode of lithium batteries at high rates and mass loadings, Chem. Eng. J. 450 (Dec. 2022) 138275, https://doi.org/10.1016/j.cej.2022.138275.
[61] Q. Liu, et al., Understanding undesirable anode lithium plating issues in lithium-ion batteries, RSC Adv. 6 (91) (Sep. 2016) 88683–88700, https://doi.org/10.1039/C6RA19482F.
[62] X. Lin, K. Khosravinia, X. Hu, J. Li, W. Lu, Lithium plating mechanism, detection, and mitigation in lithium-ion batteries, Prog. Energy Combust. Sci. 87 (Nov. 2021) 100953, https://doi.org/10.1016/j.pecs.2021.100953.
[63] N. Biju, H. Pandit, Digital twin modeling using high-fidelity battery models for state estimation and control, in: Presented at the WCX SAE World Congress Experience, Detroit, Michigan, United States, Apr. 2024, https://doi.org/10.4271/2024-01-2582, 2024-01–2582.
[64] D. Vijay, N. Framke, P. Stopp, Fast running detailed battery thermal management models based on 1D-3D synergetic approach, in: M. Bargende, H.-C. Reuss, A. Wagner (Eds.), 20. Internationales Stuttgarter Symposium, Springer Fachmedien, Wiesbaden, 2020, pp. 511–527, https://doi.org/10.1007/978-3-658-30995-4_45.